# Hydration and Ionic Conduction Mechanisms of Hexagonal Perovskite Derivatives

Sacha Fop,[1,*] James A. Dawson,[2,3] A. Dominic Fortes,[4] Clemens Ritter,[5] and Abbie C. Mclaughlin[1,*]

[1] The Chemistry Department, University of Aberdeen, Aberdeen AB24 3UE, United Kingdom

[2] Chemistry – School of Natural and Environmental Science, Newcastle University, Newcastle NE1 7RU, United Kingdom

[3] Centre for Energy, Newcastle University, Newcastle NE1 7RU, United Kingdom

[4] ISIS Facility, Rutherford Appleton Laboratory, Harwell OX11 0QX, United Kingdom

[5] Institut Laue Langevin, 38042 Grenoble, France

**ABSTRACT:** High ionic conductivity has been recently reported in hexagonal perovskite derivative materials. These systems constitute a promising class of novel electrolytes for application in hydrogen-based energy technologies. Herein, we performed the first in-situ hydration neutron diffraction experiments and atomistic calculations for the determination of the water absorption and ionic conduction mechanisms in the dual-ion conductor $Ba_7Nb_4MoO_{20}$. Our results demonstrate a remarkable mechanism of water uptake and proton incorporation, assisted by the ability of the structure of accommodating substantial stacking and anion disorder. Simulations show high dynamic and rotational flexibility of the variable coordination $MO_x$ units, a crucial factor in enabling fast ionic transport along the palmierite-like layers. Such flexibility contributes to delocalisation of the proton defects and to the creation of a frustrated proton sub-lattice with high proton mobility and low energy diffusion pathways. These insights provide design principles for the discovery of innovative ionic conductors crystallizing in related hexagonal systems or disordered oxide structures.

## Introduction

Proton and oxide ion conductors are important materials with key electrolytic applications in hydrogen-based energy conversion, storage, and electrochemical solid-state technologies. [1, 2, 3, 4, 5, 6] A crucial limitation of these technologies is the high working temperatures generally necessary for the ceramic oxide electrolyte to effectively transport the ionic species ($H^+$ or $O^{2-}$) from one electrode to the other [2, 3]. Ionic diffusion in solid oxides is strongly dependent on the characteristics of the crystal structure [7], being generally affected by the presence of structural disorder, [8, 9, 10] the existence and nature of defects, [11, 12, 13] and the flexibility of the cationic sub-lattice. [14, 15] Therefore, understanding of the relationship between structure and ionic conducting properties is fundamental for the design of electrolytes exhibiting high conductivity at reduced temperatures.

We have recently reported significant ionic conductivity in several hexagonal perovskite derivative oxides. [16, 17, 18, 19, 20, 21] Hexagonal perovskites form from mixed stacking sequences of hexagonal (h) and cubic (c) close-packing of $[AO_3]$ layers, which result in the formation of face-sharing and corner-sharing $BO_6$ octahedra. [18, 22] These hexagonal structures are extremely versatile and able to accommodate intrinsic cation and/or oxygen vacancies, enabling the ionic transport. [18, 21, 23] We have now discovered high proton and oxide ion conductivity in the cation deficient hexagonal perovskite derivative $Ba_7Nb_4MoO_{20}$. [21] $Ba_7Nb_4MoO_{20}$ presents pure proton and oxide ion conduction, and as such can be considered as a dual-ion (or mixed ion) conductor. These systems have been proposed as a new class of electrolyte for intermediate temperature ceramic fuel cells with superior performances, as they exhibit low ohmic resistance without external gas humidification. [24, 25] In dry conditions, the conductivity of $Ba_7Nb_4MoO_{20}$ is purely oxide ionic, with an oxide ion transport number, $t_{O^{2-}}$, of > 0.99 and a wide electrolytic window of $10^{-18} < pO_2 < 1$ atm at 600 °C. Proton conduction is enabled under a humidified atmosphere, thanks to the dissociative absorption of water and the creation of protonic defects. [21] $Ba_7Nb_4MoO_{20}$ exhibits proton conductivity of 4.0 mS $cm^{-1}$ at 500 °C, comparable to doped cubic barium cerate and zirconate perovskites, alongside excellent chemical and electrical stability making it attractive for practical applications.

$Ba_7Nb_4MoO_{20}$ represents the first example of high proton conduction in a hexagonal perovskite derivative. The high proton conductivity is particularly surprising as normally proton mobilities are lower in perovskite oxide structures deviating from cubic symmetry. [26, 27, 28, 29] To understand the origin of the high proton conduction in this lower symmetry hexagonal derivative, we have used a combination of in-situ neutron diffraction experiments under controlled dry/humidified air atmosphere and atomistic calculations in order to fully characterize the hydration and the ionic (proton and oxide) transport mechanisms of $Ba_7Nb_4MoO_{20}$. This is the first time that such an approach has been employed to elucidate the conduction mechanisms of a complex hexagonal perovskite derivative, providing fundamental detail on the unique ionic transport features of this important class of materials. Results show that water absorption is promoted by the ability of the cation and anion deficient hexagonal

structure of accommodating disordered environments. Disorder leads to delocalisation of the protonic defects and to high proton mobility. This demonstrates that fast proton conduction can be enabled in disordered oxide lattices and that investigation of further disordered hexagonal perovskites and oxide structures is warranted.

## Experimental section

***Synthesis and characterization.*** Samples of $Ba_7Nb_4MoO_{20}$ were synthesized by solid-state reaction method as previously reported. [21] Stoichiometric amounts of $BaCO_3$ (99.999%, Aldrich) $Nb_2O_5$ (99.99%, Aldrich) and $MoO_3$ (99.5+%, Aldrich) were ground, pressed into a pellet, heated at 1050 °C for 48h and then cooled to room temperature at 5 °C/min. The heating step was repeated until a phase pure product was obtained. Sample purity was confirmed by laboratory X-ray diffraction (XRD), while the water uptake was monitored with thermogravimetric analysis (TGA) (see Supporting Information for full details).

***Neutron diffraction and structural analysis.*** In-situ high resolution neutron diffraction experiments were performed on the time-of-flight (TOF) High Resolution Powder Diffractometer (HRPD) at ISIS (Rutherford Appleton Laboratory, Harwell, Oxford, UK). 8 g of crushed pellets of $Ba_7Nb_4MoO_{20}$ were loaded into a silica gas flow sample cell with a gas inlet/outlet allowing control of the atmosphere (see ref. 30 for details on the sample cell). Measurements were conducted under dry air and humidified air + $D_2O$ conditions. Dry conditions were produced by flowing air through a desiccant column ($pH_2O < 10^{-4}$ atm). Wet conditions were produced in an external gas mixing system by bubbling air through $D_2O$ heated at 60 °C ($pD_2O \sim 0.18$ atm). Heavy water was used instead of $H_2O$ to avoid the large incoherent neutron scattering length of the hydrogen atom. [31] Neutron diffraction data was collected on cooling the sample from 700 °C to 95 °C, with a scan time of 1.5 hours and equilibration dwell of 30 minutes at each temperature step. Additional low temperature (10 K) neutron diffraction data were collected on 3 g of a deuterated $Ba_7Nb_4MoO_{20}$ sample on the high-resolution D2B diffractometer at the Institut Laue Langevin (ILL) in Grenoble. Further details on the deuteration are reported in the Supporting Information. Neutron diffraction data were collected at $\lambda = 1.59432$ Å at 10 K and 290 K with a collection time of 3 h for each temperature.

Rietveld analysis was performed using the GSAS/EXPGUI package. [32] The average structure of $Ba_7Nb_4MoO_{20}$ as reported in ref. 21 was employed as the initial model for the Rietveld refinements. The metal Nb/Mo cations are on four different positions: M1, M2, M3 (at Wyckoff site 2*d*) and M4 (at Wyckoff site 1*b*). The oxygen atoms along the palmierite-like layers are distributed on two average partially occupied positions, O1 at Wyckoff site 6*i* and O2 at Wyckoff site 3*e*. The remaining oxygen positions (all at Wyckoff site 6*i*) are fully occupied and constitute the basal plane of the $M1O_x$ polyhedra (O3) and the M3 and M4 octahedra (O4 and O5). Ba atoms are at three different Wyckoff sites: Ba1 at 1*a*, Ba2 and Ba4 at 2*d* and Ba3 at 2*c*.

Maximum entropy (MEM) analysis was performed with the software Dysnomia, [33] employing the structure factors obtained by Rietveld refinement of the neutron diffraction data. Neutron scattering density distributions at various temperatures were reconstructed by MEM calculations with the unit cell divided into 84 x 84 x 236 pixels.

Bond-valence site energy (BVSE) calculations were performed with the *softB*V program, [34] using the structural models from Rietveld refinement as input. Bond-valence site energy landscapes for the interaction of test $H^+$ and $O^{2-}$ ions were calculated for a dense grid of points with a resolution of 0.1 Å. Energy minimum equilibrium sites and diffusion pathways were identified with regions of low bond-valence site energy by direct visualization of the isosurfaces and by examination of the calculated energy profiles.

Ellipsoidal analysis was employed to evaluate the relaxation of the average metal polyhedral units upon hydration. Analysis of minimum bonding ellipsoids was performed with the PIEFACE software.[35]

***Computational methods.*** Density functional theory (DFT) simulations were carried out with the Vienna ab initio simulation package (VASP). [36] A plane-wave cut-off energy of 520 eV and a k-point mesh spacing smaller than 0.05 $Å^{-1}$ were utilized for the geometry optimization calculations. The projector augmented wave method [37] and the PBEsol exchange-correlation functional [38] were employed for all calculations. Structures consisting of single unit cells to 2 x 2 x 2 supercells of $Ba_7Nb_4MoO_{20}$, with the number of water molecules ($nH_2O$) per formula unit equal to 0 (dehydrated), 0.125 or 0.5. Unit cell parameters and typical bond distances for the computed structures are reported in Table S1. Minimum energy path calculations between optimized and stable protonic sites were completed using the nudged elastic band (NEB) method,[39, 40] with the migration path divided into seven equidistant configurations.

Ab initio molecular dynamics (AIMD) simulations were utilized with a plane-wave cut-off energy of 400 eV and the k-space was sampled using the gamma-point only. AIMD runs of 20 ps at 1000 K using the NVT ensemble with the Nose–Hoover thermostat [41] were used to investigate oxygen-ion and proton transport in 2 x 2 x 2 $Ba_7Nb_4MoO_{20}$, $Ba_7Nb_4MoO_{20} \bullet 0.125H_2O$ and $Ba_7Nb_4MoO_{20} \bullet 0.5H_2O$ supercells containing 256, 259 and 268 ions, respectively. A time step of 1 fs was used to account for the motion of the protons. Longer AIMD simulations were prohibitively expensive as a result of the large number of valence electrons accounted for by the pseudopotentials (10 $e^-$ for Ba, 13 $e^-$ for Nb, 6 $e^-$ for Mo and 6 $e^-$ for O).

## Results and discussion

***Hydration mechanism.*** To analyse the structural changes induced by water absorption, we performed Rietveld refinement of the average $Ba_7Nb_4MoO_{20}$ structural model, which is composed by a hybrid intergrowth of oxygen deficient palmierite-like layers (cubic $[BaO_2]$) constituted by isolated polyhedral units and 12R hexagonal perovskite blocks (space group $P\bar{3}m1$) (Figure 1a). $Ba_7Nb_4MoO_{20}$ can uptake a considerable amount of water, up to $\sim 0.80$ $H_2O$ molecules per formula unit as demonstrated by thermogravimetric analysis (Figure S1). Water absorption generally occurs via the hydration of oxygen vacancies ($H_2O_{(g)} + V_O^{\bullet\bullet} + O_O^X \leftrightarrow 2OH_O^\bullet$) and results in the creation of protonic defects. [26] In the average structure, the intrinsic oxygen

vacancies along the palmierite-like layer are randomly distributed on the partially occupied O1/O2 sites (Figure 1), resulting in the formation of average tetrahedral M1($O3_3O1$) and octahedral M1($O3_3O2_3$) units. Refinement of the O1 and O2 partial occupancies without any constraint shows that the O1 site is predominantly occupied under dry conditions (Figure 2a; also see Table S2 for the full results of the structural refinements and Figure S2 for the fitted neutron diffraction histograms).

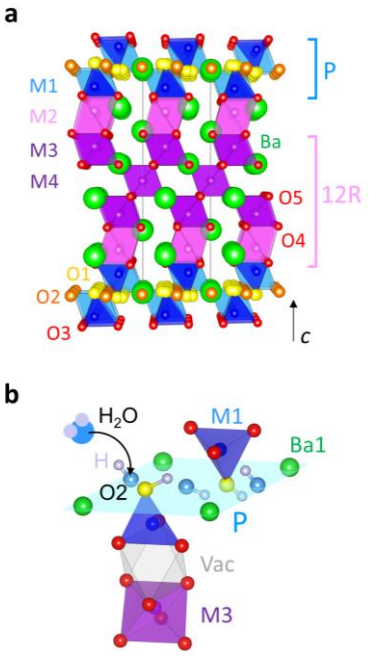


**Figure 1.** a) Average crystal structure of $Ba_7Nb_4MoO_{20}$ composed of an intergrowth of palmierite-like layers (P) and 12R hexagonal perovskite blocks. Blue and light blue polyhedral represent the variable geometry $M1O_x$ units with average tetrahedral and octahedral coordination created by partial occupation of the two crystallographic oxygen positions O1 and O2. The M1 and M2 metal positions are also partially occupied, thus resulting in hybrid trimer stackings of cationic vacancies and isolated/face-sharing polyhedral units. b) Representation of the water absorption on the vacant O2 site along the cubic [$Ba1O_2$] plane of the palmierite-like layer. Vac indicates a vacant M2 site.

There is a small reorganization of the fractional occupancies above 300 °C, with a further increase in the O1 fractional occupancy and concomitant decrease in O2, so that the O2 site is empty above 500 °C. Under humidified conditions, the O1 fractional occupancy refined to ≥ 0.333. The full occupancy value of this site is 1/3, thus the occupancy of O1 was set to 0.333. The O2 fractional occupancy in humidified air is considerably larger than in dry conditions and increases on reducing the temperature following a nonlinear behaviour with a steep change in slope at 300 °C. Comparison between the values of the O1/O2 fractional occupancies in dry and humidified atmosphere attests unambiguously that water absorption occurs via hydration of the intrinsic oxygen vacancies on the cubic [$BaO_2$] plane of the palmierite-like layer (Figure 1b). Water is predominantly absorbed on the average O2 crystallographic position. In dry conditions, the oxygen vacancies are mostly distributed on the O2 sites, which are then filled by water molecules under a humidified atmosphere. It is worth noticing that the interstitial oxygen atom in the doped $Ba_7Nb_{3.9}Mo_{1.1}O_{20.05}$ composition occupies the same average octahedral site, [42] confirming a similar oxygen defect incorporation mechanism and providing additional evidence for the structural flexibility of the palmierite-like layers.

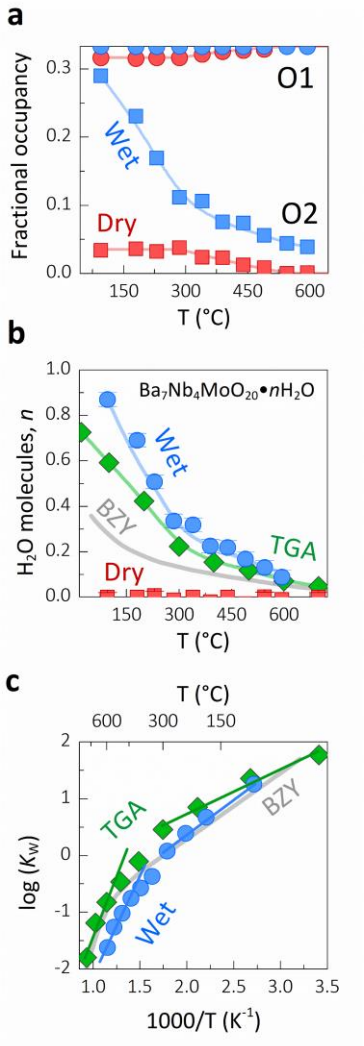


**Figure 2.** a) Variation of the O1 and O2 oxygen fractional occupancies in dry and humidified conditions. b) Number of hydrated molecules, *n*, calculated from the excess oxygen incorporated in the $Ba_7Nb_4MoO_{20}$ • $nH_2O$ structure and measured by equilibrium isotherms with thermogravimetric analysis under humidified air. c) Equilibrium constant for the water absorption reaction. Lines correspond to the linear fit to the data. Water concentration and equilibrium constant of $Ba_3Zr_{0.8}Y_{0.2}O_{3-\delta}$ (BZY) from ref. 43 are reported in b and c for comparison.

The number of water molecules, *n*, in hydrated $Ba_7Nb_4MoO_{20} \bullet nH_2O$ can be inferred from the amount of excess oxygen incorporated in the palmierite-like layer. Refining the oxygen site occupancies in the structure of the dehydrated material resulted in an overall oxygen stoichiometry of ~ $O_{20.00}$ and $n \sim 0$ throughout the entire temperature range (Figure 2b). At 595 °C, $n = 0.09$ for the hydrated material. As the temperature decreases, the value of *n* increases up to $n = 0.87$ at 95 °C, close to the theoretical solubility limit of one water molecule per formula unit. The number of absorbed water molecules obtained from the in-situ neutron diffraction experiments is in good agreement with the thermogravimetric measurements. There is a clear change in the rate of water uptake below 300 °C, suggesting two different hydration regimes. Assuming that the corresponding number of protons should be present to preserve charge neutrality, the equilibrium constant ($K_W$) of the water absorption reaction can be calculated from the amount of excess oxygen (see Supporting Information for details). The thermal variation of the equilibrium constant is shown in Figure 2c. There is a clear nonlinear behaviour with a gradual change in slope above 300 °C. By fitting the variation of $\log(K_w)$ against 1/T it is possible to obtain the hydration enthalpy and entropy. For T < 300 °C, $\Delta H^0$ = -24 kJ mol$^{-1}$ and $\Delta S^0$ = -41 J K$^{-1}$ mol$^{-1}$; at higher temperatures, $\Delta H^0$ = -67 kJ mol$^{-1}$ and $\Delta S^0$ = -94 J K$^{-1}$ mol$^{-1}$. These values are in agreement with the ones obtained from thermogravimetric analysis (T < 300 °C, $\Delta H^0$ = -18 kJ mol$^{-1}$ and $\Delta S^0$ = -31 J K$^{-1}$ mol$^{-1}$; T > 300 °C, $\Delta H^0$ = -76 kJ mol$^{-1}$ and $\Delta S^0$ = -101 J K$^{-1}$ mol$^{-1}$) and in a previous report, [21] and are in line with values from well-known proton conductors. [26, 43, 44]

DFT calculations were also used to determine the hydration enthalpy of $Ba_7Nb_4MoO_{20}$ based on the energy differences between the hydrated and dehydrated materials, as reported for other proton conductors. [45, 46] In ~~excellent~~ agreement with our experimental findings, the calculated hydration enthalpies are between -96 and -1 kJ mol$^{-1}$ and are strongly dependent on the moisture content, proton locations and orientations and M1/M2 occupancy, as shown in Table S3. Our simulations reveal a slight energetic preference for protonation of the O1 sites, although there are only small differences (< 15 kJ mol$^{-1}$) between the hydration enthalpies for protons at the distinct O1 and O2 sites. In addition, as shown in Table S3, we find that occupancy of the M2 site results in strongly exothermic hydration enthalpies for protons located between the O1 site and the M1 vacancy. This is particularly noteworthy because our calculations also show that in the dry material, the occupation of a single M2 site is 55 kJ mol$^{-1}$ less favourable than the occupation of a single M1 site. This explain why M2 occupation is unfavoured in the dry material and suggests that there is a strong favourable interaction between protons and vacant M1 sites which has important implications for the proton conductivity (as described later).

***Hydration and structural disorder.*** In order to locate the proton (deuteron) positions, low temperature (10 K) neutron diffraction data were collected on a deuterated $Ba_7Nb_4MoO_{20} \bullet nD_2O$ sample on the high-resolution diffractometer D2B. Refinement of the oxygen O1 and O2 fractional occupancies resulted in an oxygen stoichiometry of $O_{20.37}$, indicating a $D_2O$ concentration of n = 0.37. Difference Fourier maps were used to locate missing scattering density from the deuterium atoms. Inspection of the difference Fourier map at 10 K reveals missing scattering density on the palmierite-like layer at (~ 0.30, ~ 0.46, ~ 0.98), corresponding to Wyckoff position 12j (Figure 3a).

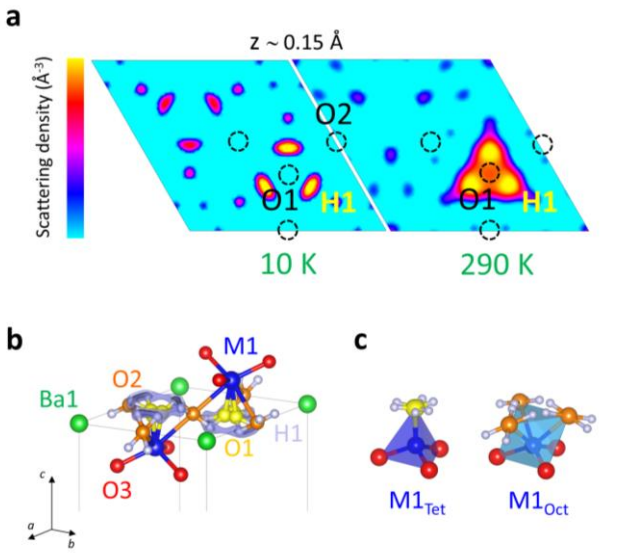


**Figure 3.** a) Difference Fourier maps at $z \sim 0.15$ Å from origin as seen along the [001] direction at 10 K and 290 K. b) Proton (deuteron) equilibrium positions along the palmierite-like layers. Bond-valence site energy isosurfaces showing the lowest BVS energy equilibrium proton position (0.0 eV, darker isosurface) together with the low energy connectivity area around O1 (< 0.10 eV, lighter isosurface) are superimposed for comparison. c) Proton positions in relation to the average M1 tetrahedral and octahedral units.

Inclusion of a deuteron on this site (H1) with a fixed occupancy corresponding to the level of hydration resulted in a stable refinement with the statistics factors reducing from $\chi^2 = 4.53$, $R_p = 4.80\%$, $R_{wp} = 5.90\%$ to $\chi^2 = 3.36$, $R_p = 3.92\%$, $R_{wp} = 4.71\%$ and in an excellent match between the calculated and observed profiles (see Table S4 and Figure S4). The deuteron is located in proximity of the average O1 and O2 sites, on six equivalent positions (Figure 3b, c). The average bond lengths are O1–H1 ~0.95 - 1.11 Å and O2–H1 ~1.10 Å, in line with values determined in other proton conducting oxides. [47, 48, 49] Refinement of the structure from the neutron data collected at 290 K leads to similar results. Comparison between the difference Fourier maps reveals that the proton positions are delocalized at 290 K (Figure 3a), suggesting a distribution of available proton locations around the 12j equilibrium site as the temperature increases. This is confirmed by bond-valence sum energy (BVSE) analysis performed with a test $H^+$ ion, which together with the lowest energy (0.0 eV, absolute energy minimum) equilibrium position at H1 evidences an area of low energy (< 0.10 eV) connectivity around O1 (Figure 3b).

The Fourier map in Figure 3a and the BVSE results suggests that protons in $Ba_7Nb_4MoO_{20}$ are delocalized and can reside in various positions around the equilibrium site H1. To determine the lowest energy proton sites using DFT, single protons were placed at various locations around O1 and O2 sites and then geometry optimized. As previously explained, our calculations demonstrate that protons energetically prefer to sit on the O1 site and so we focus our discussion on this site. For protons residing on O1, three different general scenarios were found, as displayed in Figure 4a (these three scenarios also generally apply to the O2 sites).

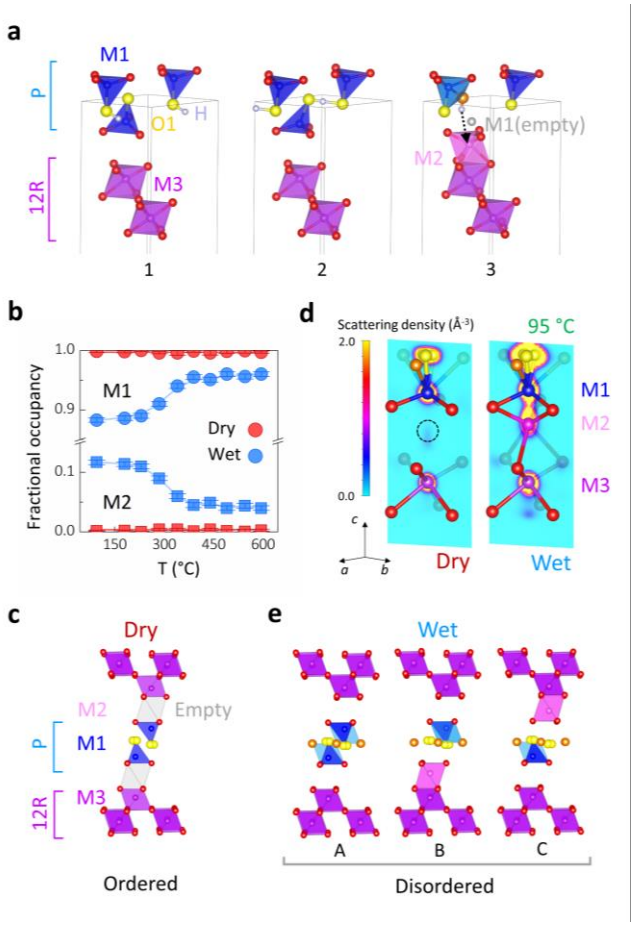


**Figure 4.** a) Representation of typical proton configurations around O1 as obtained by DFT geometry optimization calculations. b) Thermal variation of the M1 and M2 fractional occupancies obtained by refinement of the $Ba_7Nb_4MoO_{20}$ structure from the in-situ HRPD neutron diffraction data. c) Ordered palmierite-12R stacking in dry $Ba_7Nb_4MoO_{20}$. d) Maximum entropy (MEM) maps showing the nuclear scattering density distribution at 95 °C on the M1-M2-M3 vertical (at $x \sim 0.667$) as seen along the [100] direction. e) Disordered metal-vacancy stacking configurations in hydrated $Ba_7Nb_4MoO_{20}$.

Scenario 1 features a proton located in the standard H1 location. Scenario 2 illustrates a proton positioned between two neighbouring oxygen atoms and effectively represents a transition state for proton hopping. In the third scenario, the proton is positioned between an oxygen site and an M1 site, which forces occupation of the previously vacant M2 site. The M1 cation now appears to be 5-fold with the protonated oxygen moved from O1 closer to a O2 site. As discussed previously, this scenario is very energetically favorable (large exothermic hydration enthalpy), as a result of the strong interaction between the proton and vacant M1 site. The fact that we see such a substantial structural change through a geometric optimization clearly indicates a strong relationship between the uptake of water and M1/M2 site occupation in this material.

Refinement of the M1 and M2 fractional occupancies from the HRPD in-situ neutron data reveals that in dry air the M1 site is fully occupied (> 0.997) while the M2 site is empty (Figure 4b and Supporting Table S2). The cationic vacancies are ordered on the M2 site so that the average structure is comprised by an ordered intergrowth of palmierite-like layers and 12R hexagonal perovskite units spaced by a layer of empty octahedral sites (Figure 4c), as originally reported by García-González et al. [50] The hydrated sample on the contrary shows partial occupation of both the M1 and M2 sites (Figure 4b). As previously demonstrated, the repulsion between a proton pointing towards the nearest $M1O_x$ unit and the M1 cation (scenario 3 in Figure 4a) drives the shift of the metal atom from M1 to the empty M2 site, with consequent local disordering of the cationic vacancies. A similar influence of the protonic defects on the cation sub-lattice has been reported for the layered hexagonal perovskite oxyhydroxide $Ba_4Ru_3O_{10.2}(OH)_{1.8}$. [51] Maximum entropy (MEM) analysis of the neutron diffraction data, which minimizes bias imposed by the structural model, [11, 52] confirms occupation of the M2 site in the hydrated material, while the site is clearly empty in dry air (Figure 4d). This result is further corroborated by difference Fourier maps calculated at 95 °C (Figure S4). The MEM analysis shows that the scattering density at M2 is dependent on the water absorption, increasing as the temperature is lowered (Figure S5). The continuous distribution between M1 and M2 at the lower temperatures indicates disordering and dynamic exchange between the two sites. These results clearly demonstrate that occupation of the M2 site, and hence disordering of the cationic vacancies, is induced by the water absorption in agreement with the DFT calculations. Due to the short separation (< 1.5 Å), the M1 and M2 sites are mutually exclusive, so that only two sites per M1-M2-M3 trimer can be simultaneously occupied. This results in a disordered metal-vacancy stacking distribution, with different local configurations creating a complex average network of isolated, face-sharing and corner-sharing polyhedral units (Figure 4e). Similar stacking disordering has been reported in the related hexagonal perovskite derivatives $Ba_3M'M''O_{8.5}$, [19, 53] although its origins have never been investigated. $Ba_3MoNbO_{8.5}$ can also uptake a significant amount of water within the palmierite layers, [21] therefore we carried out DFT simulations to determine whether proton incorporation can have a similar influence on the cation vacancy distribution in these systems. Results from geometry optimization of a single proton in $Ba_3MoNbO_{8.5}$ show that when a proton is bound to an oxygen site of an $NbO_4$ unit, the tetrahedrally coordinated Nb ion shifts to an octahedral $NbO_6$ coordination, similar to the case of $Ba_7Nb_4MoO_{20}$ (Figure S6). This behaviour was also confirmed for $MoO_4$. These results suggest that stacking disordering in $Ba_3M'M''O_{8.5}$ derivatives is

induced by the water absorption, indicating that this phenomenon is common to cation deficient hexagonal perovskite families containing palmierite-like layers. Such a rare structural phenomenon is enabled by the flexibility of the cationic sub-lattice and facilitates water incorporation.

In the average structure of $Ba_7Nb_4MoO_{20}$, the short O1–O2 separation (< 2.0 Å) does not allow the simultaneous occupation of the two crystallographic oxygen sites, thus leading to positional oxygen disorder and the formation of $M1O_x$ units with mixed local 4-, 5-, and 6-fold coordination (Figure S7a). [21] Hydration of the oxygen vacancies leads to further disruption of the average coordination environment and to an increase in positional disorder, as demonstrated by MEM analysis and by the correlation of the isotropic displacement parameter for the O1 and O2 atoms with the water absorption (Figure S7b,c). The particular topology of the palmierite-like layers, together with the ability of the M1 centres of adopting variable coordination, allows the accommodation of more disordered and distorted local polyhedral geometries, importantly promoting the water absorption.

Water absorption in the layered $Ba_7Nb_4MoO_{20}$ structure occurs anisotropically, and results in disordering and consequent induced strain in certain directions of the lattice (Figure S8 and Figure S9). Upon hydration, $Ba_7Nb_4MoO_{20}$ exhibits a complex structural relaxation, the signature of which is also evident in the nonlinear behaviour of the unit cell parameters for the hydrated material (Figure S10). Similar trends have been reported in various related $Ba_3M'M''O_{8.5}$ materials and have been associated to changes in the oxygen populations and to different occupation of the cation sites. [54, 55, 56] Overall, our in-situ neutron diffraction experiments and DFT calculations demonstrate that water is clearly responsible for the unusual variation of the crystal structures with temperature and a main driver of the cation and anion disorder exhibited by these cation deficient hexagonal derivatives. These results also confirm the intrinsic structural flexibility of these systems, as further highlighted by a recent variable pressure study on $Ba_3NbMoO_{8.5}$ which revealed a low bulk modulus closer in magnitude to that of the halide perovskites. [57] In cubic perovskite systems, any reduction in symmetry reduces the water solubility. [26] In contrast, the significant structural flexibility of hexagonal $Ba_7Nb_4MoO_{20}$ allows the accommodation of substantial local cation and anion disorder, a key factor in enabling a high concentration of water uptake. This suggests that other hexagonal perovskites derivatives and layered systems containing palmierite motifs with flexible structures may be prime candidates for proton conduction.

***Ionic conduction mechanisms.*** Both the proton and oxide ion conduction mechanism were investigated by ab initio molecular dynamics (AIMD) simulations at 1000 K. Oxygen diffusion is primarily restricted to two dimensions in the palmierite layers, as illustrated by the oxide ion trajectory plots in Figure 5a for the dry material. Even for the relatively short simulation time of 20 ps, the hopping between adjacent O1 sites is still visible, as highlighted by the black dashed circles in Figure 5a.

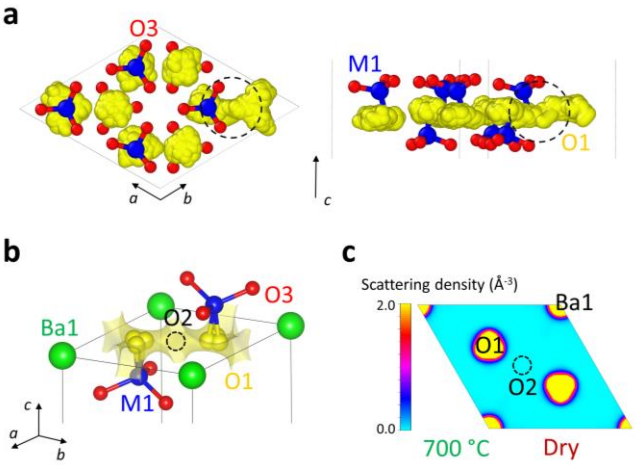


**Figure 5.** a) Oxide ion trajectory plot for dry $Ba_7Nb_4MoO_{20}$ obtained by AIMD simulations at 1100 K. The black dashed circle highlights hopping between adjacent O1 sites. b) Bond-valence site energy map showing the oxide ion conduction pathway formed by the lowest energy connecting isosurfaces for an $O^{2-}$ ion along the palmierite-like layer in dry $Ba_7Nb_4MoO_{20}$. Isosurface levels are drawn at < 0.4 eV over the global minimum. c) Maximum entropy (MEM) maps showing the nuclear scattering density distribution for dry $Ba_7Nb_4MoO_{20}$ at 700 °C at $z$ = 0 as seen along the [001] direction.

The ionic pathways were confirmed by bond-valence site energy (BVSE) calculations of the interaction of a probe oxide ion in the refined structural model of the dry material with the O2 site empty. Lowest bond-valence site energy connectivity is evidenced along the palmierite-like layers (Figure 5b), implying a curved conduction pathway involving the O1 site and the empty O2 crystallographic position, in agreement with the AIMD simulations. The O2 site in dry $Ba_7Nb_4MoO_{20}$ is empty above 500 °C, and MEM analysis of the dry structure at 700 °C reveals no continuous scattering density distribution between adjacent O1 sites (Figure 5c), which would be consistent with a direct single particle mechanism for oxygen diffusion. [11] This mechanism differs from the one reported for doped $Ba_7Nb_{3.9}Mo_{1.1}O_{20.05}$ (and the related $Ba_3NbMoO_{8.5}$ oxide ion conductor), where occupation of the average octahedral O2 site by the interstitial oxygen atom leads to a cooperative (interstitialcy) diffusion mechanism. [42, 54, 58] The partial occupation of O2 suggests that cooperative tetrahedral-octahedral interchange may also be present in $Ba_7Nb_4MoO_{20}$ at low temperatures, when both O1 and O2 are occupied. These results demonstrate the inherent flexibility of the palmierite-like layers of supporting various types of oxide ion transport: single particle vacancy mediated hopping and cooperative-intestitialcy diffusion. [59]

AIMD simulations of $Ba_7Nb_4MoO_{20} \bullet 0.125H_2O$ and $Ba_7Nb_4MoO_{20} \bullet 0.5H_2O$ were also used to probe proton hopping. The proton trajectory plots are given in Figure 6a. The proton hops several times between three oxide ions in the palmierite layer during the 20 ps simulation. This is in

agreement with the lowest energy (~ 0.14 eV) proton percolation pathway along the palmierite-like layer obtained by calculation of the BVSE landscape for the interaction of a probe $H^+$ ion in the refined average structural model of the hydrated material (Figure 6b; also see Figure S11 for the full energy landscape and pathways). This mechanism involves rotation of the protons around the O1 and O2 positions and hopping onto an H1 site on an adjacent M1 centre. We calculated the mean squared displacement (MSD) for protons during the AIMD simulations (Figure S12), and obtained proton diffusion coefficients of $8.90 \times 10^{-6}$ and $1.82 \times 10^{-5}$ $cm^2\ s^{-1}$ at 1000 K for $Ba_7Nb_4MoO_{20} \bullet 0.125H_2O$ and $Ba_7Nb_4MoO_{20} \bullet 0.5H_2O$, respectively. These values are very similar to those obtained for other well-known proton-conducting perovskites, such as $BaCeO_3$ and $BaZrO_3$, [60, 61] resulting in a comparable proton conductivity (see Figure S13), which further illustrates the potential of this material in fuel cell applications.

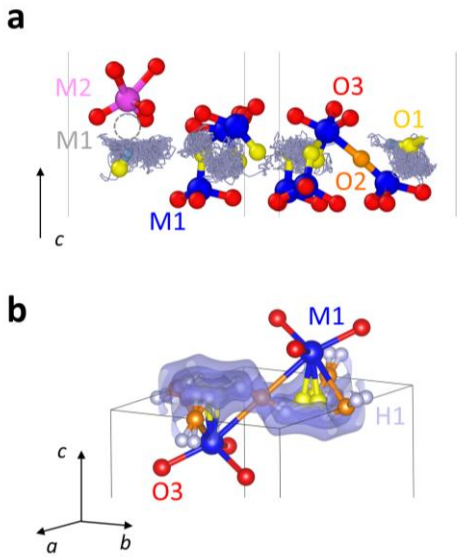


**Figure 6.** a) Proton trajectory plots for hydrated $Ba_7Nb_4MoO_{20} \bullet 0.5H_2O$ obtained by AIMD simulations. A proton in proximity of an empty M1 site (indicated by the gray dotted circle) does not undergo any hopping for the duration of the simulation. b) BVSE map calculated for a test $H^+$ ion for hydrated $Ba_7Nb_4MoO_{20}$ showing connectivity along the palmierite-like layer (isosurface levels < 0.15 eV).

It is noteworthy that a proton in vicinity of a vacant M1 site is trapped for the duration of the simulation and does not undergo a single hop, while the others exhibit long-range hopping (Figure 6a). This supports our previous observation of a strong interaction between oppositely charged protons and M1 vacancies. The trapping of protons by M1 vacancies was further confirmed using NEB calculations to determine the migration energy barrier for a proton hopping from an oxygen site adjacent to an M1 vacancy (scenario 3 in Figure 4c) to a neighbouring H1 location. The energy profile for such a hop is presented in Figure S14 with a calculated migration energy of 0.61 eV (similar to the experimental value of 0.57 eV). [21] This large barrier indicates the strong trapping of protons by M1 vacancies and also explains why this configuration is so stable, as discussed above. In contrast, for the reverse hop from a standard H1 location to an oxygen neighbouring an M1 vacancy, the barrier is substantially lower at 0.18 eV, again illustrating the energetic benefit of a proton neighbouring an M1 vacancy. Based on the results of our calculations (Figure S14), we estimate the trapping energy to be > 0.4 eV, which is larger than that reported for other well-known proton conductors, such as Y-doped $BaZrO_3$ (0.3 eV). [45, 62]

Proton trapping provides an explanation for the unusual temperature variation of the proton transport number and the reduced proton mobility in $Ba_7Nb_4MoO_{20}$ below 300 °C. [21] The concentration of cationic vacancies on the M1 site is larger (M2 more occupied) below 300 °C (Figure 4b). The atomistic simulations clearly show that the vacancies on the M1 site act as traps for the protonic defects, inhibiting any long-range proton hopping. Therefore, the larger number of M1 vacancies effectively results in a reduction of the protonic conduction below 300 °C. The cationic vacancies on M1 decrease between 300 and 400 °C, and this rearrangement leads to a sharp increase in the protonic contribution from ~ 20% to ~ 80%, with a 300% increase of the proton conductivity in respect to the oxide ion conductivity (see Supporting Figure S15). [21] Such an increase in the protonic contribution is highly unusual. The proton conduction component in oxides usually decreases with the temperature due to thermal dehydration. These results suggest that the proton and oxide ion components may be tailored via control of the geometry of the M1/M2 cations by chemical substitution. [19, 56]

To further understand the local structural factors that influence the ionic transport in $Ba_7Nb_4MoO_{20}$, we have analysed the radial distribution functions (RDFs) of various ion pairs during the AIMD simulations of $Ba_7Nb_4MoO_{20} \bullet 0.5H_2O$. The M–O RDF for the $M1O_4$ tetrahedron has a single peak at 1.82 Å (Figure 7a). It is noteworthy that this peak exhibits strong broadening at *r* values up to 2.4 Å, which is indicative of significant M–O stretching in these tetrahedra. Similar behaviour is also observed for the equivalent RDF of a $M2O_6$ octahedron, as well as for a $M1O_5$ polyhedron, albeit to a less extent. In contrast, this broadening is not observed for the RDF of the individual $M3O_6$ units. These findings suggest that the $MO_x$ polyhedral units in the palmerite-like layers exhibit greater flexibility than the rigid $M3O_6$ octahedra in the perovskite blocks. The O–O RDFs confirm such flexibility (Figure S16a), which is also highlighted by the inherent disorder of the palmierite-like layers when compared to the 12R perovskite blocks (Figure S16b).

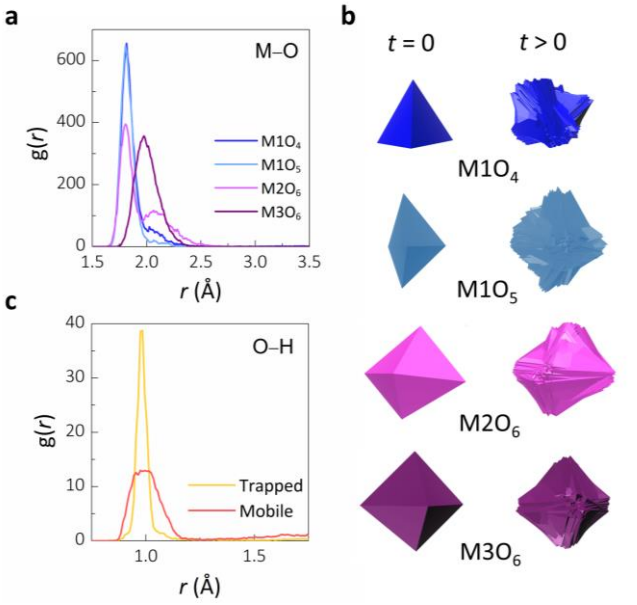


**Figure 7.** a) M–O radial distribution functions (RDFs) for the individual metal polyhedral units for hydrated $Ba_7Nb_4MoO_{20}$ • $0.5H_2O$. b) Schematic showing the orientations of the different $MO_x$ polyhedral units at the start ($t$ = 0) and for every timestep ($t$ > 0) of the AIMD simulations overlaid on each other. c) O–H RDFs for a single proton trapped by an M1 vacancy and for a single mobile proton.

Figure 7b shows the orientations of the different polyhedra for every timestep of the AIMD simulation overlaid on each other, which can be used to visually assess whether particular polyhedra can rotate or not in $Ba_7Nb_4MoO_{20}$. It is clear that the $M1O_4$ tetrahedron can rotate in the material. The $M1O_5$ polyhedron also exhibits significant rotation, whereas both the $M2O_6$ and $M3O_6$ octahedra are more rigid with very limited rotation. The inherent dynamic flexibility of the variable $MO_X$ coordination units along the palmierite-like layers determines the high ionic conductivity of this hexagonal system. Similarly to the case of other oxide ion conductors containing isolated tetrahedral moieties, [14, 15] fast oxide ion migration in dry $Ba_7Nb_4MoO_{20}$ is enabled by the dynamic and rotational flexibility of the $M1O_x$ units and by the ability of the metal centres of adopting variable coordination environments. The rotational motion of the $M1O_x$ units also assists the proton motion in hydrated $Ba_7Nb_4MoO_{20}$, as in the case of the solid-acid protonic conductor $CsH_2PO_4$. [63]

Proton diffusion is usually slower in lower symmetry perovskite oxides such as orthorhombic $SrCeO_3$ and $CaZrO_3$, due to an additional enthalpy contribution needed for tilting of neighbouring octahedra close enough to allow proton hopping. [26, 27] In addition, localisation of the protonic defects generally leads to reduced proton conductivity, as in the case of the 6H hexagonal phase of Sc-doped $BaTiO_{3-\delta}$ when compared to the cubic phase. [28, 29] In hydrated $Ba_7Nb_4MoO_{20}$, the positional oxide ion disorder generated by the close proximity of available oxygen sites due to the particular topology of the palmierite layers, together with the dynamic flexibility of the $M1O_x$ units, result in delocalisation of the protonic defects (as demonstrated by the difference Fourier maps in Figure 3 and the DFT and BVSE calculations), and in a broad range of O–H distances, as demonstrated by the RDF of the O–H pairs for a mobile proton (Figure 7c). The similar energies of the different proton configurations lead to a disordered proton sub-lattice, where frustration of the proton positions (and of the hydrogen bond network) coupled with the dynamic flexibility of the metal units result in high mobility of the protonic defects and in the creation of low energy transport pathways. [63, 64, 65]

## Conclusions

In-situ neutron diffraction experiments in combination with atomistic calculations have been used to elucidate the mechanisms of hydration and ionic transport for the first time in the cation deficient hexagonal perovskite $Ba_7Nb_4MoO_{20}$. The water uptake occurs by filling of the intrinsic oxygen vacancies distributed along the palmierite-like layers and predominantly located at the average O2 site in the dry structure. Our results demonstrate that the hydration process is a main driver of the cation and anion disorder seen in $Ba_7Nb_4MoO_{20}$ and related hexagonal perovskite derivative conductors. The water absorption is responsible for disordering of the metal-vacancy stacking distribution and contributes to the positional oxygen disorder along the palmierite-like layers. Both the oxide ion and proton transports are two dimensional, occurring along the palmierite-like layers, and are assisted by the inherent flexibility of the $MO_x$ units and the accessibility of available oxygen positions. Protons are highly delocalized over a variety of configurations, resulting in a frustrated proton sub-lattice with high mobility of the protonic defects and low energy diffusion pathways. Overall, our findings demonstrate that water absorption and high ionic mobility are promoted in $Ba_7Nb_4MoO_{20}$ thanks to the ability of the crystal lattice of accommodating anion and cation disordered environments and to the dynamic and rotational flexibility of the oxygen-deficient palmierite layers. The example of $Ba_7Nb_4MoO_{20}$ suggests that candidate materials with cation deficient layers or palmierite-like motifs in the vast family of hexagonal perovskite derivatives are likely to support significant oxide ion and/or proton conduction. [22, 66, 67, 68, 69, 70, 71] Importantly, the insights presented here demonstrates that fast proton conduction can be enabled by disordered solid oxide systems (in contrast with conventional cubic perovskite conductors where ionic transport is promoted by the high symmetry of the crystal lattice) and provides innovative design rules for the development of solid electrolytes crystallizing in oxides with disordered sub-lattices.

## ASSOCIATED CONTENT

**Supporting Information**. The supporting information includes further experimental details, thermogravimetric data, figures and tables of crystallographic data, figures showing electrical data, figures and tables of further results of DFT and AIMD calculations. This material is available free of charge via the Internet at http://pubs.acs.org.

## AUTHOR INFORMATION

**Corresponding Authors**

*** Sacha Fop**; orcid.org/0000-0003-4168-6363;
Email: sacha.fop1@abdn.ac.uk

*** Abbie C. Mclaughlin**; orcid.org/0000-0001-9960-723X;
Email: a.c.mclaughlin@abdn.ac.uk

**Authors**

**James A. Dawson**; orcid.org/0000-0002-3946-5337

**Dominic Fortes**; orcid.org/0000-0001-5907-2285

**Clemens Ritter**

**Funding Sources**

This research was supported by the Leverhulme-Trust (RPG-2017-351).

**Notes**

The authors declare no competing financial interest.

**ACKNOWLEDGMENT**

S.F. and A.C.M. acknowledge STFC-GB for provision of beamtime at ISIS (DOI: 10.5286/ISIS.E.RB1920006) and the ILL. J.A.D. gratefully acknowledges the EPSRC and the MCC/Archer consortium (EP/L000202/1) for computational resources. J.A.D. also gratefully acknowledges Newcastle University for funding through a Newcastle Academic Track (NUAcT) Fellowship.

## REFERENCES


[1] Steele, B. C.; Heinzel. A. Materials for fuel-cell technologies. *Nature* **2001**, *414*, 345-352.

[2] Wachsman, E. D.; Lee, K. T. Lowering the Temperature of Solid Oxide Fuel Cells. *Science* **2011**, *334*, 935-939.

[3] Duan, C.; Tong, J.; Shang, M.; Nikodemski, S.; Sanders, M.; Ricote, S.; Almansoori, A.; O'Hayre, R. Readily Processed Protonic Ceramic Fuel Cells with High Performance at Low Temperatures. *Science* **2015**, *349*, 1321-1326.

[4] Choi, S.; Kucharczyk, C. J.; Liang, Y.; Zhang, X.; Takeuchi, I.; Ji, H.; Haile, S. M. Exceptional Power Density and Stability at Intermediate Temperatures in Protonic Ceramic Fuel Cells. *Nature Energy* **2018**, *3*, 202-210.

[5] Duan, C.; Kee, R.; Zhu, H.; Sullivan, N.; Zhu, L.; Bian, L.; Jennings, D.; O'Hayre, R. Highly efficient reversible protonic ceramic electrochemical cells for power generation and fuel production. *Nature Energy* **2019**, *4*, 230-240.

[6] Marnellos, G.; Stoukides, M. Ammonia Synthesis at Atmospheric Pressure. *Science* **1998**, *282*, 98.

[7] Malavasi, L.; Fisher, C. A. J.; Islam, M. S. Oxide-Ion and Proton Conducting Electrolyte Materials for Clean Energy Applications: Structural and Mechanistic Features. *Chem. Soc. Rev.* **2010**, *39*, 4370-4387.

[8] Abraham, F.; Boivin, J. C.; Mairesse, G.; Nowogrocki, G. The Bimevox Series: A New Family of High Performances Oxide Ion Conductors. *Solid State Ionics* **1990**, *40-41*, 934-937.

[9] Evans, I. R.; Howard, J. A. K.; Evans, J. S. O. The Crystal Structure of α-$La_2Mo_2O_9$ and the Structural Origin of the Oxide Ion Migration Pathway. *Chem. Mater.* **2005**, *17*, 4074-4077.

[10] Mohn, C. E.; Stølen, S.; Norberg, S. T.; Hull, S. Oxide-Ion Disorder Within the High Temperature δ Phase of $Bi_2O_3$. *Phys. Rev. Lett.* **2009**, *102*, 155502.

[11] Kuang, X.; Green, M. A.; Niu, H.; Zajdel, P.; Dickinson, C.; Claridge, J. B.; Jantsky, L.; Rosseinsky, M. J. Interstitial Oxide Ion Conductivity in the Layered Tetrahedral Network Melilite Structure. *Nat. Mater.* **2008**, *7*, 498-504.

[12] Mather, G. C.; Fisher, C. A. J.; Islam, M. S. Defects, Dopants, and Protons in $LaNbO_4$. *Chem. Mater.* **2010**, *22*, 5912-5917.

[13] Yang, X.; FernÃ¡ndez-Carrión, A. J.; Wang, J.; Porcher, F.; Fayon, F.; Allix, M.; Kuang, X. Cooperative Mechanisms of Oxygen Vacancy Stabilization and Migration in the Isolated Tetrahedral Anion Scheelite Structure. *Nat. Commun.* **2018**, *9*, 4484.

[14] Kendrick, E.; Kendrick, J.; Knight, K. S.; Islam, M. S.; Slater, P. R. Cooperative Mechanisms of Fast-Ion Conduction in Gallium-Based Oxides with Tetrahedral Moieties. *Nat. Mater.* **2007**, *6*, 871-875.

[15] Kuang, X.; Payne, J. L.; Johnson, M. R.; Radosavljevic Evans, I. Remarkably High Oxide Ion Conductivity at Low Temperature in an Ordered Fluorite-Type Superstructure. *Angew. Chem. Int. Ed.* **2012**, *51*, 690-694.

[16] Fop, S.; Skakle, J. M. S.; McLaughlin, A. C.; Connor, P. A.; Irvine, J. T. S.; Smith, R. I.; Wildman, E. J. Oxide Ion Conductivity in the Hexagonal Perovskite Derivative $Ba_3MoNbO_{8.5}$. *J. Am. Chem. Soc.* **2016**, *138*, 16764-16769.

[17] McCombie, K. S.; Wildman, E. J.; Fop, S.; Smith, R. I.; Skakle, J. M.S.; Mclaughlin, A. C. The Crystal Structure and Electrical Properties of the Oxide Ion Conductor $Ba_3WNbO_{8.5}$. *J. Mater. Chem. A* **2018**, *6*, 5290-5295.

[18] Fop, S.; McCombie, K. S.; Wildman, E. J.; Skakle, J. M. S.; Mclaughlin, A. C. Hexagonal Perovskite Derivatives: A New Direction in the Design of Oxide Ion Conducting Materials. *Chem. Commun.* **2019**, *55*, 2127-2137.

[19] Fop, S.; McCombie, K.; Smith, R. I.; Mclaughlin, A. C. Enhanced Oxygen Ion Conductivity and Mechanistic Understanding in $Ba_3Nb_{1-x}V_xMoO_{8.5}$. *Chem. Mater.* **2020**, *32*, 4724-4733.

[20] Gilane, A.; Fop, S.; Sher, F.; Smith, R. I.; Mclaughlin, A. C. The Relationship Between Oxide-Ion Conductivity and Cation Vacancy Order in the Hybrid Hexagonal Perovskite $Ba_3VWO_{8.5}$. *J. Mater. Chem. A* **2020**, *8*, 16506-16514.

[21] Fop, S.; McCombie, K. S.; Wildman, E. J.; Skakle, J. M. S.; Irvine, J. T. S.; Connor, P. A.; Savaniu, C.; Ritter, C.; Mclaughlin, A. C. High Oxide Ion and Proton Conductivity in a Disordered Hexagonal Perovskite. *Nat. Mater.* **2020**, *19*, 752-757.

[22] Darriet, J.; Subramanian, M. A. Structural Relationships Between Compounds Based on the Stacking of Mixed Layers Related to Hexagonal Perovskite-Type Structures. *J. Mater. Chem.* **1995**, *5*, 543-552.

[23] Murakami, T.; Hester, J. R.; Yashima, M. High Proton Conductivity in $Ba_5Er_2Al_2ZrO_{13}$, a Hexagonal Perovskite-Related Oxide with Intrinsically Oxygen-Deficient Layers. *J. Am. Chem. Soc.* **2020**, *142*, 11653-11657.

[24] Yang, L.; Wang, S.; Blinn, K.; Liu, M.; Liu, Z.; Cheng, Z.; Liu, M. Enhanced Sulfur and Coking Tolerance of a Mixed Ion Conductor for SOFCs: $BaZr_{0.1}Ce_{0.7}Y_{0.2-x}Yb_xO_{3-\delta}$. *Science* **2009**, *326*, 126-1229.

[25] Zhou, C.; Sunarso, J.; Song, Y.; Dai, J.; Zhang, J.; Gu, B.; Zhou, W.; Shao, Z. New Reduced-temperature Ceramic Fuel Cells with Dual-ion Conducting Electrolyte and Triple-conducting Double Perovskite Cathode. *J. Mater. Chem. A* **2019**, *7*, 13265-13274.

[26] Kreuer, K. D. Proton-Conducting Oxides. *Annu. Rev. Mater. Res.* **2003**, *33*, 333–359.

[27] Islam, M. S. Ionic Transport in $ABO_3$ Perovskite Oxides: A Computer Modelling Tour. *J. Mater. Chem.* **2000**, *10*, 1027-1038.

[28] Rahman, S. M. H.; Norberg, S. T.; Knee, C. S.; Biendicho, J. J.; Hull, S.; Eriksson, S. G. Proton conductivity of hexagonal and cubic $BaTi_{1-x}Sc_xO_{3-\delta}$ ($0.1 \le x \le 0.8$). *Dalton Trans.* **2014**, *43*, 15055-15064.

[29] Torino, N.; Henry, P. F.; Knee, C. S.; Bjørheim, T. S.; Rahman, S. M. H.; Suard, E.; Giacobbe, C.; Eriksson, S. G. The Influence of Cation Ordering, Oxygen Vacancy Distribution and Proton Siting on Observed Properties in Ceramic Electrolytes: The Case of Scandium Substituted Barium Titanate. *Dalton Trans.* **2017**, *46*, 8387-8398.

[30] Haynes, R.; Norberg, S. T.; Eriksson, S. G.; Chowdhury, M. A. H.; Goodway, C. M.; Howells, G. D.; Kirichek, O.; Hull, S. New High Temperature Gas Flow Cell Developed at ISIS. *Journal of Physics: Conference Series* **2010**, *251*, 012090.

[31] Sears, V. F. Neutron scattering lengths and cross sections. *Neutron News* **1992**, *3*, 26-37.

[32] Toby, B. H. EXPGUI a graphical user interface for GSAS. *Journal of Applied Crystallography* **2001**, *34*, 210-213.

[33] Momma, K.; Ikeda, T.; Belik, A. A.; Izumi, F. Dysnomia, a Computer Program for Maximum-Entropy Method (MEM) Analysis and its Performance in the MEM-Based Pattern Fitting. *Powder Diffraction* **2013**, *28*, 184-193.

[34] Chen, H.; Wong, L. L.; Adams, S. SoftBV - a Software Tool for Screening the Materials Genome of Inorganic Fast Ion Conductors. *Acta Crystallographica Section B* **2019**, *75*, 18-33.

[35] Cumby, J.; Attfield, J. P. Ellipsoidal Analysis of Coordination Polyhedra. *Nat. Commun.* **2017**, *8*, 14235.

[36] Kresse, G.; Furthmüller, J. Efficient Iterative Schemes for Ab Initio Total-Energy Calculations Using a Plane-Wave Basis Set. *Phys. Rev. B: Condens. Matter Mater. Phys.* **1996**, *54*, 11169–11186.

[37] Blöchl, P. E. Projector Augmented-Wave Method. *Phys. Rev. B: Condens. Matter Mater. Phys.* **1994**, *50*, 17953–17979.

[38] Perdew, J. P.; Ruzsinszky, A.; Csonka, G. I.; Vydrov, O. A.; Scuseria, G. E.; Constantin, L. A.; Zhou, X.; Burke, K. Restoring the Density-Gradient Expansion for Exchange in Solids and Surfaces. *Phys. Rev. Lett.* **2008**, *100*, 136406.

[39] Henkelman, G.; Jonsson, H. Improved Tangent Estimate in the´ Nudged Elastic Band Method for Finding Minimum Energy Paths and Saddle Points. *J. Chem. Phys.* **2000**, 113, 9978–9985.

[40] Sheppard, D.; Terrell, R.; Henkelman, G. Optimization Methods for Finding Minimum Energy Paths. *J. Chem. Phys*. **2008**, 128, 134106.
[41] D.J. Evans, B.L. Holian, The Nose–Hoover Thermostat, *J. Chem. Phys*. **1985**, *83*, 4069–4074.
[42] Yashima, M.; Tsujiguchi, T.; Sakuda, Y.; Yasui, Y.; Zhou, Y.; Fujii, K.; Torii, S.; Kamiyama, T.; Skinner, S. J. High Oxide-Ion Conductivity Through the Interstitial Oxygen Site in $Ba_7Nb_4MoO_{20}$-based Hexagonal Perovskite Related Oxides. *Nat. Commun.* **2021**, *12*, 556.
[43] Yamazaki, Y.; Babilo, P.; Haile, S. M. Defect Chemistry of Yttrium-Doped Barium Zirconate: A Thermodynamic Analysis of Water Uptake. *Chem. Mater.* **2008**, *20*, 6352-6357.
[44] Haugsrud, R.; Norby, T. Proton Conduction in Rare-earth Orthoniobates and Ortho-tantalates. *Nat. Mater.* **2006**, *5*, 193-196.
[45] Dawson, J. A.; Miller, J. A.; Tanaka, I. First-Principles Insight into the Hydration Ability and Proton Conduction of the Solid State Proton Conductor, Y and Sn Co-Doped $BaZrO_3$. *Chem. Mater.* **2015**, *27*, 901–908.
[46] Hermet, J.; Torrent, M.; Bottin, F.; Dezanneau, G.; Geneste, G. Hydrogen Diffusion in the Protonic Conductor $BaCe_{1-x}Gd_x O_{3-x/2}$ from Density Functional theory. *Phys. Rev. B* **2013**, *87*, 104303.
[47] Eriksson Andersson, A. K.; Selbach, S. M.; Grande, T.; Knee, C. S. Thermal Evolution of the Crystal Structure of Proton Conducting $BaCe_{0.8}Y_{0.2}O_{3-\delta}$ From High-Resolution Neutron Diffraction in Dry and Humid Atmosphere. *Dalton Trans.* **2015**, *44*, 10834-10846
[48] Mather, G. C.; Heras-Juaristi, G.; Ritter, C.; Fuentes, R. O.; Chinelatto, A. L.; Pérez-Coll, D.; Amador, U. Phase Transitions, Chemical Expansion, and Deuteron Sites in the $BaZr_{0.7}Ce_{0.2}Y_{0.1}O_{3-\delta}$ Proton Conductor. *Chem. Mater.* **2016**, *28*, 4292-4299.
[49] Kendrick, E.; Knight, K. S.; Islam, M. S.; Slater, P. R. Structural Studies of the Proton Conducting Perovskite '$La_{0.6}Ba_{0.4}ScO_{2.8}$'. *Solid State Ionics* **2007**, *178*, 943-949.
[50] García-González, E.; Parras, M.; González-Calbet, J. M. Crystal Structure of an Unusual Polytype: 7H-$Ba_7Nb_4MoO_{20}$. *Chem. Mater.* **1999**, *11*, 433-437.
[51] Hiley, C. I.; Lees, M. R.; Hammond, D. L.; Kashtiban, R. J.; Sloan, J.; Smith, R. I.; Walton, R. I. $Ba_4Ru_3O_{10.2}(OH)_{1.8}$: a New Member of the Layered Hexagonal Perovskite Family Crystallised from Water. *Chem. Commun.* **2016**, *52*, 6375-6378.
[52] Yashima, M.; Sirikanda, N.; Ishihara, T. Crystal Structure, Diffusion Path, and Oxygen Permeability of a $Pr_2NiO_4$-Based Mixed Conductor $(Pr_{0.9}La_{0.1})_2(Ni_{0.74}Cu_{0.21}Ga_{0.05})O_{4+\delta}$. *J. Am. Chem. Soc.* **2010**, *132*, 2385-2392.
[53] Auckett, J. E.; Milton, K. L.; Evans, I. R. Cation Distributions and Anion Disorder in $Ba_3NbMO_{8.5}$ (M = Mo, W) Materials: Implications for Oxide Ion Conductivity. *Chem. Mater.* **2019**, *31*, 1715-1719.
[54] Fop, S.; Wildman, E. J.; Irvine, J. T. S.; Connor, P. A.; Skakle, J. M. S.; Ritter, C.; Mclaughlin, A. C. Investigation of the Relationship between the Structure and Conductivity of the Novel Oxide Ionic Conductor $Ba_3MoNbO_{8.5}$. *Chem. Mater.* **2017**, *29*, 4146-4152.
[55] Chambers, M. S.; McCombie, K. S.; Auckett, J. E.; McLaughlin, A. C.; Irvine, J. T. S.; Chater, P. A.; Evans, J. S. O.; Evans, I. R. Hexagonal Perovskite Related Oxide Ion Conductor $Ba_3NbMoO_{8.5}$: Phase Transition, Temperature Evolution Of The Local Structure And Properties. *J. Mater. Chem. A* **2019**, *7*, 25503-25510.
[56] Coduri, M.; Bernasconi, A.; Fischer, H. E.; Malavasi, L. The $Ba_3Mo_{1-x}W_xNbO_{8.5}$ Ion Conductors: Insights into Local Coordination from X-Ray and Neutron Total Scattering. *J. Mater. Chem. A* **2020**, *8*, 21227-21240.
[57] Sherwood, B.; Ridley, C. J.; Bull, C. L.; Fop, S.; Skakle, J. M. S.; McLaughlin, A. C.; Wildman, E. J. A pressure induced reversal to the 9R perovskite in $Ba_3MoNbO_{8.5}$. *J. Mater. Chem. A* **2021**, *9*, 6567-6574.
[58] Yashima, M.; Tsujiguchi, T.; Fujii, K.; Niwa, E.; Nishioka, S.; Hester, J. R.; Maeda, K. Direct Evidence for Two-Dimensional Oxide-Ion Diffusion in the Hexagonal Perovskite-Related Oxide $Ba_3MoNbO_{8.5-\delta}$. *J. Mater. Chem. A* **2019**, *7*, 13910-13916.
[59] Yang, X.; Fernández-Carrión, A. J.; Wang, J.; Porcher, F.; Fayon, F.; Allix, M.; Kuang, X. Cooperative Mechanisms of Oxygen Vacancy Stabilization and Migration in the Isolated Tetrahedral Anion Scheelite Structure. *Nat. Commun.* **2018**, *9*, 4484.
[60] Münch, W.; Kreuer, K. -.; Seifert, G.; Maier, J. Proton Diffusion in Perovskites: Comparison Between $BaCeO_3$, $BaZrO_3$, $SrTiO_3$, and CaTiO3 Using Quantum Molecular Dynamics. *Solid State Ionics* **2000**, *136-137*, 183-189
[61] Kreuer, K. D. On the Complexity of Proton Conduction Phenomena. *Solid State Ionics* **2000**, *136-137*, 149-160.
[62] Yamazaki, Y.; Blanc, F.; Okuyama, Y.; Buannic, L.; Lucio-Vega, J. C.; Grey, C. P.; Haile, S. M. Proton Trapping in Yttrium-Doped Barium Zirconate. *Nat. Mater*. **2013**, *12*, 647–651.
[63] Kim, G.; Griffin, J. M.; Blanc, F.; Haile, S. M.; Grey, C. P. Characterization of the Dynamics in the Protonic Conductor $CsH_2PO_4$ by $^{17}O$ Solid-State NMR Spectroscopy and First-Principles Calculations: Correlating Phosphate and Protonic Motion. *J. Am. Chem. Soc.* **2015**, *137*, 3867-3876.
[64] Vilčiauskas, L.; Tuckerman, M. E.; Bester, G.; Paddison, S. J.; Kreuer, K. The Mechanism of Proton Conduction in Phosphoric Acid. *Nature Chemistry* **2012**, *4*, 461-466.
[65] Islam, M. S.; Nolan, A. M.; Wang, S.; Bai, Q.; Mo, Y. A Computational Study of Fast Proton Diffusion in Brownmillerite $Sr_2Co_2O_5$. *Chem. Mater.* **2020**, *32*, 5028-5035.
[66] Mössner, B.; Kemmler-Sack, S. 8H-perowskitstapelvarianten in den Systemen BaO⍰$B^{3+}_2O_3$⍰$TiO_2$⍰$Nb_2O_5$ (B = In, Lu, Yb). *Journal of the Less Common Metals* **1986**, *120*, 203-211.
[67] Zhang, H.; Wu, Y.; Meng, S.; Fang, L. Crystal Structure and Microwave Dielectric Properties of a New $A_4B_3O_{12}$-type cation-deficient perovskite $Ba_3LaTa_3O_{12}$. *J. Alloys Compounds* **2008**, *460*, 460-463.
[68] Bezjak, J.; Jančar, B.; Boullay, P.; Rečnik, A.; Suvorov, D. Hexagonal Perovskite-Type Phases in the BaO-Rich Part of the BaO–$WO_3$–$Nb_2O_5$ System. *J Am Ceram Soc* **2009**, *92*, 3022-3032.
[69] Kuang, X.; Jing, X.; Loong, C.; Lachowski, E. E.; Skakle, J. M. S.; West, A. R. A New Hexagonal 12-Layer Perovskite-Related Structure: $Ba_6R_2Ti_4O_{17}$ (R = Nd and Y). *Chem. Mater.* **2002**, *14*, 4359-4363.
[70] Skakle, J. M. S.; Coats, A. M.; Marr, J. The Crystal Structures of $Ba_2R_{2/3}V2O_8$ (R = La, Nd) and $Sr_2La_{2/3}V_2O_8$; Palmierite Derivatives. *J. Mater. Sci.* **2000**, *35*, 3251-3256.
[71] Wildman, E. J.; Mclaughlin, A. C.; Macdonald, J. F.; Hanna, J. V.; Skakle, J. M. S. The Crystal Structure of $Ba_3Nb_2O_8$ Revisited: A Neutron Diffraction and Solid-State NMR Study. *Inorg. Chem.* **2017**, *56*, 2653-2661.

Insert Table of Contents artwork here

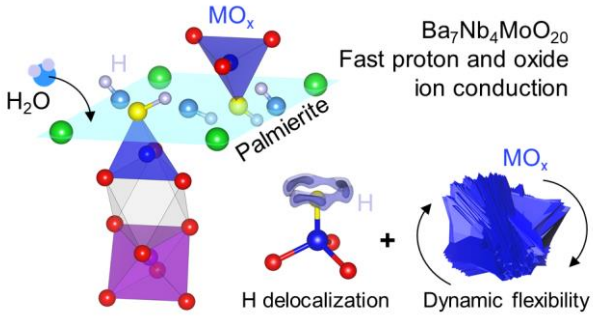
MO$_x$
H
H$_2$O
Palmierite
Ba$_7$Nb$_4$MoO$_{20}$
Fast proton and oxide
ion conduction
MO$_x$
H
+
H delocalization
Dynamic flexibility